

Synthesis and characterization of aluminum-doped tin oxide nanoparticles for aerospace applications

S. Sharma ^a, K. S. Yamuna ^b, S. Sheeba Rani ^c, B. Sangeetha ^d, S. Sivakumar ^{e,*},
B. Esther Bharathi ^e, L. Guru Prasad ^f

^a Department of Electronics and communication Engineering, New Horizon College of Engineering, Bengaluru, Karnataka, India

^b Department of Electrical and Electronics Engineering, Sona College of Technology, Salem, Tamilnadu, India.

^c Department of Electronics and communication Engineering, Sri Eshwar College of Engineering, Coimbatore, Tamilnadu, India.

^d Department of Electrical and Electronics Engineering, AVS Engineering College, Salem, Tamilnadu, India.

^e Department of Physics, Government Arts College (Autonomous), Salem, Tamilnadu, India.

^f Department of Physics, Mangalore Institute of Technology and Engineering, Mangalore, Karnataka, India

Aluminium doped Tin Oxide (ATO) nanoparticles were synthesized using the sol-gel method and analysed for structural, morphological and optical properties. X-ray diffraction (XRD) confirmed the successful incorporation of Al³⁺ ions into the SnO₂ lattice, retaining its tetragonal rutile structure. The shifts in diffraction peaks to higher 2θ values indicated lattice contraction due to the smaller ionic radius of Al³⁺ compared to Sn⁴⁺. Scanning electron microscopy (SEM) revealed a uniform particle distribution with reduced agglomeration. UV-Visible spectroscopy exhibited a hypsochromic shift in the absorption edge, attributed to bandgap widening caused by aluminium doping. Fourier Transform Infrared (FTIR) spectroscopy identified characteristic vibrational modes of functional groups, confirming chemical bonding. Photoluminescence (PL) studies showed enhanced emission intensities due to oxygen vacancies and electronic interactions between Al dopants and the SnO₂ lattice, suggesting defect state creation. The tailored structural and optical properties enhance ATO's potential in gas sensors utilised in aerospace engines.

(Received February 26, 2025; Accepted June 2, 2025)

Keywords: Nanoparticles, SnO₂, Al, Lattice strain, Optical properties, Optoelectronics

1. Introduction

Tin oxide (SnO₂) has gained significant attention in recent years due to its promising properties for various applications, including optoelectronics, photocatalysis, gas sensing and transparent conductive films. However, the pure SnO₂ material often exhibits limitations, such as high resistivity and suboptimal optical properties, which delay its performance in many applications. To overcome these challenges, doping SnO₂ with various elements has become a common strategy for tuning its properties. Among the various dopants, Aluminium (Al) has been widely studied due to its smaller ionic radius and ability to modify the electronic structure and optical properties of SnO₂, leading to improved performance in diverse fields. ATO nanoparticles synthesized via the sol-gel method have been extensively investigated and their structural, electronic and optical properties have been found to be significantly influenced by the doping concentration. The incorporation of Al³⁺ ions into the SnO₂ lattice induces lattice contraction, altering the material's electronic band structure and improving its optical response. Various studies have demonstrated that Al doping can lead to modifications in the absorption edge, increase in the

* Corresponding author: sivaphotonics@gmail.com

<https://doi.org/10.15251/DJNB.2025.202.585>

material's photocatalytic activity and enhanced gas sensing properties. These effects are attributed to the creation of oxygen vacancies, defect states and changes in the electronic interaction between the dopant ions and the SnO₂ lattice.

In recent years, several studies have focused on optimizing the synthesis conditions and doping concentrations of ATO to enhance its properties for specific applications. It has been reported that the doping of SnO₂ with aluminium enhances its transparency and conductivity, making it suitable for use in transparent conductive films and its photocatalytic efficiency for dye degradation and water splitting [1]. Other works have focused on the gas-sensing properties of ATO, where it has been found that Al doping improves the sensitivity and selectivity toward various gases, such as NO₂ and CO [2,3].

The structural characterization of ATO nanoparticles is typically carried out using X-ray diffraction (XRD), which provides insight into the crystallinity and lattice parameters of the material. Studies have shown that Al doping induces lattice contraction and changes the crystallite size [4]. Scanning electron microscopy (SEM) and Transmission electron microscopy (TEM) are also commonly used to investigate the surface morphology and particle size distribution of ATO nanoparticles [5]. Optical properties are often analysed using UV-Visible spectroscopy and doping induced modifications in the absorption spectra have been reported, with a shift in the absorption edge attributed to the modification of the bandgap [6]. Photoluminescence (PL) studies have also highlighted the role of oxygen vacancies and dopant induced defects in enhancing the emission properties of ATO nanoparticles [7].

This study explores the synthesis of ATO nanoparticles, along with their structural and optical characterization. The investigation emphasizes the role of aluminium doping in tailoring the properties of SnO₂, with a focus on the interplay between doping concentration and insights from PL studies, FTIR spectroscopy and SEM.

2. Synthesis of the ATO nanoparticles

ATO nanoparticles were synthesised using the sol-gel method [8-13], a precursor solution is first prepared. Tin chloride pentahydrate (SnCl₂·5H₂O) is dissolved in absolute ethanol to form a 1M solution and the mixture is stirred for 30 minutes to ensure complete dissolution. Aluminium chloride hexahydrate (AlCl₃·6H₂O) is added to the solution to achieve a doping concentration of approximately 5wt.%. The mixture is stirred vigorously for an additional 60 minutes to ensure homogenous mixing and dissolution of the aluminium salt. To initiate the gelation process, a stoichiometric amount of water and a few drops of nitric acid (HNO₃) are added to the solution and the mixture is stirred continuously for 4-6 hours. The resulting sol is then allowed to age for 24 hours, allowing the polymerization to proceed. The gel obtained is dried in an oven at 80°C for 12 hours, followed by calcination at 500°C for 4 hours to obtain the ATO nanoparticles. The calcined product is then cooled to room temperature and stored in a desiccator for further analysis [14,15].

3. Characterization methods

The structure of the synthesized ATO nanoparticles was analyzed using X-ray diffraction (XRD) with a Rigaku Mini Flex 600 desktop diffractometer, utilizing CuK α radiation (wavelength 1.5406 Å). FTIR spectroscopy was employed to identify functional groups within the wavenumber range of 400cm⁻¹ to 4000cm⁻¹, using a Perkin Elmer Spectrum II with a spectral resolution of 0.5 cm⁻¹ and wavelength accuracy of 0.1 cm⁻¹ at 4000 cm⁻¹. The optical properties and energy band gap were evaluated through UV-Vis spectroscopy, recorded on a Perkin Elmer Lambda 950 spectrophotometer with a wavelength accuracy of ± 0.08 nm, covering the range from 200 nm to 800 nm. Photoluminescence (PL) measurements were conducted using a Horiba Jobin Yvon spectrometer, with a 325 nm He-Cd laser serving as the excitation source. The morphology and surface features of the nanoparticles were examined via a Jeol 7001F Field Emission SEM.

4. Results and discussions

4.1. Structural analysis

The X-ray diffraction (XRD) pattern of ATO nanoparticles, as illustrated in Figure 1, demonstrates clear reflections at 2θ values of 27.31° , 34.79° , 38.99° and 53.22° . These peaks correspond to the (110), (101), (200) and (211) crystallographic planes, respectively, characteristic of the tetragonal rutile phase of SnO_2 (JCPDS card No. 41-1445). Additional minor peaks indexed to the (111) and (220) planes of aluminium (JCPDS card No. 65-2869), highlight the contribution of aluminium within the material matrix. The distinct presence of these peaks suggests the successful incorporation of Al^{3+} ions into the SnO_2 lattice.

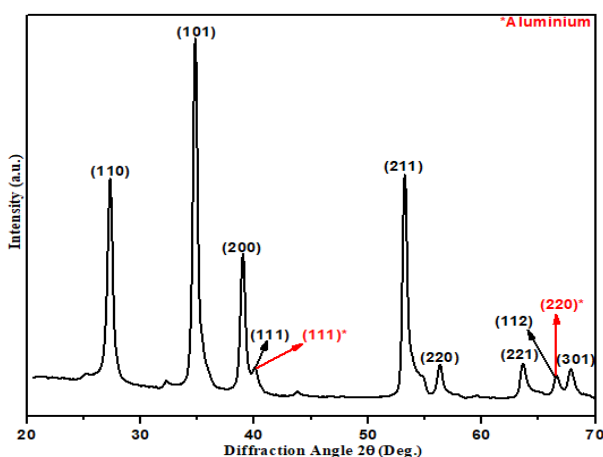


Fig. 1. XRD Pattern of ATO nanoparticles.

The substitution of Sn^{4+} ions by Al^{3+} ions, due to their smaller ionic radius (0.053 nm compared to 0.069 nm), induces a contraction of the unit cell, leading to peak shifts toward higher 2θ angles. This phenomenon indicates lattice shrinkage, a direct consequence of doping. The absence of any peaks corresponding to Al_2O_3 or other aluminium related phases further confirms that Al^{3+} ions integrate seamlessly into the SnO_2 lattice rather than forming secondary phases [16]. This uniform incorporation validates the sol-gel method's effectiveness in producing a homogeneous doped structure under optimized synthesis conditions. Furthermore, aluminium doping introduces substantial lattice strain and defects, as evidenced by peak broadening in the XRD pattern. These defects disrupt the long-range crystalline order, inhibit crystallite growth and reduce crystallite size, a conclusion supported by Scherrer's equation analysis. The strain-induced distortions are dependent on the doping concentration and contribute significantly to the observed structural changes. Bragg's law calculations reveal a systematic reduction in the lattice parameters 'a' and 'c,' aligning with the anticipated lattice contraction. The crystallite size has been determined from the XRD data,

$$D = \frac{k\lambda}{\beta \cos\theta} \text{ (nm)}$$

The dislocation density (δ) can be obtained as

$$\delta = \frac{15\beta \cos\theta}{4\alpha D} \text{ lines / m}^2$$

Micro strain (ϵ) can be calculated from,

$$\varepsilon = \frac{\beta}{4\cos\theta}$$

The relationship between the stacking fault probability (α) and the peak shifts (β) is described by the following expression.

$$\alpha = \left[\frac{2\pi^2}{45(3\tan\theta)^{\frac{1}{2}}} \right] \beta(\text{\AA})$$

Table 1. Structural parameters of ATO nanoparticles.

Planes	Crystalline Size (nm)	Dislocation Density (10^{15} lines/m ²)	Stacking Fault Probability (\AA)	Elastic Strain
110	14.73	7.7079	0.0052	0.0104
101	17.35	5.5535	0.0040	0.0070
200	18.66	4.8005	0.0035	0.0058
211	20.19	4.1034	0.0029	0.0040

From Table 1, the crystalline size of ATO nanoparticles for the (110) plane is determined to be 14.73 nm, the smallest among the analysed planes, indicating significant structural modifications due to doping. The substitution of Sn⁴⁺ ions with smaller Al³⁺ ions leads to lattice contraction, pulling surrounding atoms closer and reducing lattice parameters. This contraction introduces localized strain, measured as 0.0104, which disrupts the lattice's long-range periodicity, inhibiting crystallite growth and resulting in reduced crystalline size.

The dislocation density for the (110) plane is calculated as 7.7079×10^{15} lines/m², the highest among the planes, indicating a significant increase in structural imperfections. Stacking fault probability, at 0.0052 \AA , further confirms the presence of disruptions in the stacking sequence of crystal planes. These defects act as barriers to crystallite growth by creating energy sinks and limiting atomic mobility during synthesis. The combined effects of increased strain, higher dislocation density and stacking fault probability prevent the coalescence of smaller crystallites into larger domains. These values highlight the structural changes induced by aluminium doping, significantly impacting the crystalline structure.

The structural alterations induced by aluminium doping, including the interplay of lattice contraction, strain and defects, not only tailor the electronic band structure and reduce crystalline size but also enhance the material's optical and electronic properties, underscoring its suitability for potential applications in optoelectronics, gas sensors, photocatalysis and transparent conductive films.

4.2. FTIR analysis

FTIR spectroscopy provides crucial information about the structural and chemical properties of ATO nanoparticles, as shown in Figure 2. The observed vibrational modes correspond to specific chemical bonds and functional groups, offering a detailed understanding of the material's composition and structural characteristics. The spectrum recorded in the range of 400-4000 cm⁻¹, reveals significant vibrational modes corresponding to functional groups and metal-oxide bonding. A broad band centered around ~ 3395 cm⁻¹ is attributed to the stretching vibrations of surface hydroxyl (-OH) groups and adsorbed water molecules [17], indicative of the hydrophilic nature and surface activity of the nanoparticles.

Peaks in the region of 1300-1500 cm⁻¹ are linked to the symmetric and asymmetric stretching of organic residues or carbonyl groups, likely remnants of the sol-gel synthesis process. These peaks provide evidence of the interaction between precursor materials and solvents during the formation of the doped nanoparticles. Characteristic peaks associated with the SnO₂ lattice are prominent in the lower wavenumber region. The strong peak at ~ 478 cm⁻¹ corresponds to the Sn-O bond stretching, confirming the formation of the tin oxide matrix. The peak near ~ 917 cm⁻¹ is attributed to Sn-O-Sn bridging vibrations, reflecting the integrity of the tetragonal rutile structure.

Additionally, weak absorptions below 500 cm^{-1} , such as those near $\sim 450\text{ cm}^{-1}$, further validate metal-oxygen interactions critical to the material's crystallinity.

Interestingly, no distinct peaks for Al-O bonds are detected, suggesting that Al^{3+} ions are successfully substituted into the SnO_2 lattice without forming separate Al_2O_3 phases. The absence of aluminium oxide signatures, coupled with the consistent Sn-O bonding peaks, confirms the efficient incorporation of aluminium into the tin oxide framework. This incorporation introduces lattice distortions, influencing the physical and chemical properties of the material. The comprehensive FTIR analysis underscores the structural integrity, chemical homogeneity and effectiveness of the doping process, positioning Al:SnO₂ as a versatile material for advanced applications.

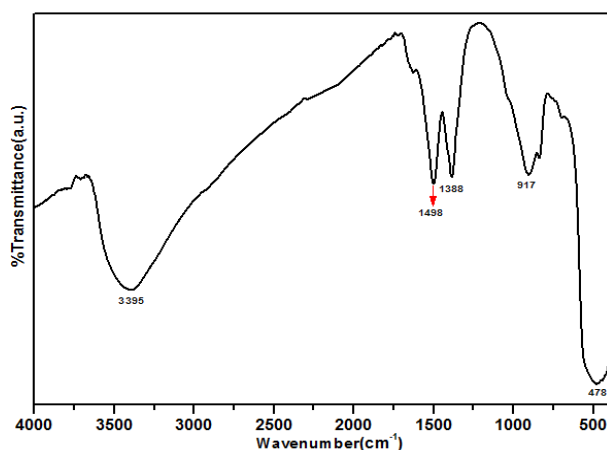


Fig. 2. FTIR Spectrum of ATO nanoparticles.

4.3. Optical properties

The UV-Vis absorbance spectra of ATO nanoparticles, shown in Figure 3, exhibit a prominent absorption peak at 321nm, indicating the material's efficient light-harvesting capability in the ultraviolet (UV) region. This absorption feature is attributed to intrinsic electronic transitions within the SnO_2 lattice, with the doping of Al^{3+} ions modulating these transitions by introducing defect states, specifically oxygen vacancies, which further enhance optical absorption and provide additional electronic pathways.

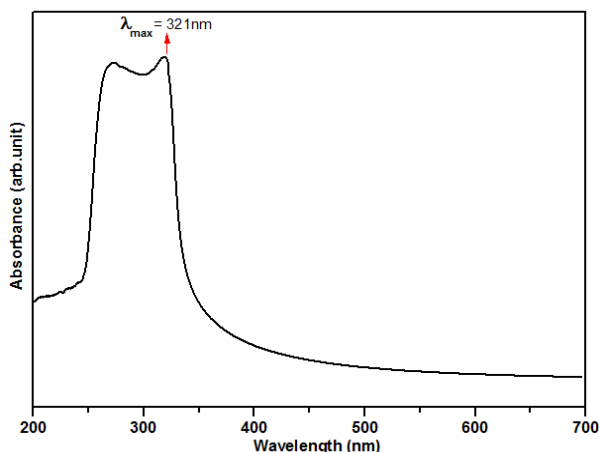


Fig. 3. UV-Vis absorbance spectra of ATO nanoparticles.

The absorbance at 321nm corresponds to the excitation of electrons from valence band to conduction band. This increases free charge carriers, enhancing conductivity and sensor response. This shift corresponds to an increase in the optical bandgap, which is estimated to be approximately 3.7 eV (Figure 4), compared to 3.6 eV for undoped SnO₂ [18].

Whenever the Oxygen molecules (O₂) from air capture free electrons, forming negatively charged oxygen species (O₂⁻, O⁻, O²⁻) modulates the sensor's resistance. When an oxidizing gas like NO₂ interacts with these adsorbed oxygen species, it further traps electrons, leading to an increase in resistance. Conversely, when reducing gases like CO, H₂, or CH₄ react with the adsorbed oxygen, trapped electrons are released back into the conduction band, decreasing resistance and increasing conductivity. This enables faster, more sensitive detection of fuel leaks, emissions and air quality fluctuations in aerospace propulsion systems.

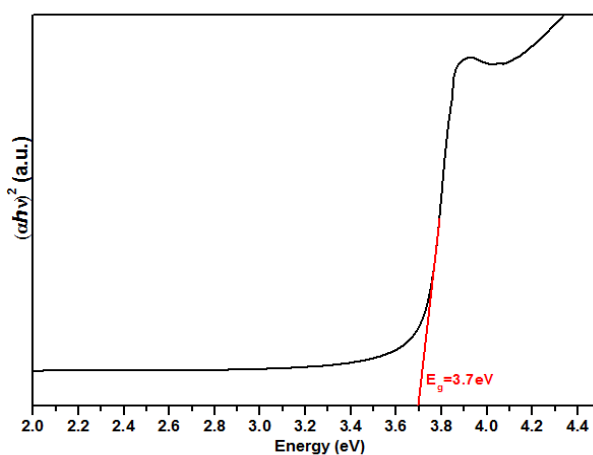


Fig. 4. Bandgap Energy of ATO nanoparticles.

4.4. Photoluminescence studies

The photoluminescence spectrum of ATO nanoparticles exhibits two prominent emission peaks, indicating different electronic transitions and defect-related recombination pathways shown in Figure 5. The first peak, located around ~320nm, corresponds to the band-to-band transition, where electrons excited from the valence band (HOMO) relax back to the conduction band (LUMO) via radiative recombination [16]. This emission confirms the bandgap energy of approximately 3.7 eV, consistent with UV-Vis absorption analysis. This transition is a result of fluorescence, arising from a spin-allowed and fast recombination process between the conduction band minimum and valence band maximum. The second peak, observed in the visible region 500 nm, is attributed to defect-mediated transitions. These emissions involve electron transitions from localized defect states to the valence band. The defect states act as intermediate energy levels within the bandgap, enabling recombination pathways at lower energy. The slower de-excitation process associated with these defect levels suggests contributions from phosphorescence, where spin-forbidden transitions between triplet defect states and the valence band occur. In terms of HOMO-LUMO specifications, the first peak is related to direct recombination between the HOMO and the LUMO, while the second peak involves intermediate trap states that modify the effective electronic transitions [19]. The dual peaks highlight the influence of aluminium doping in altering the electronic structure and introducing defect-related energy levels that enhance luminescence in the visible region.

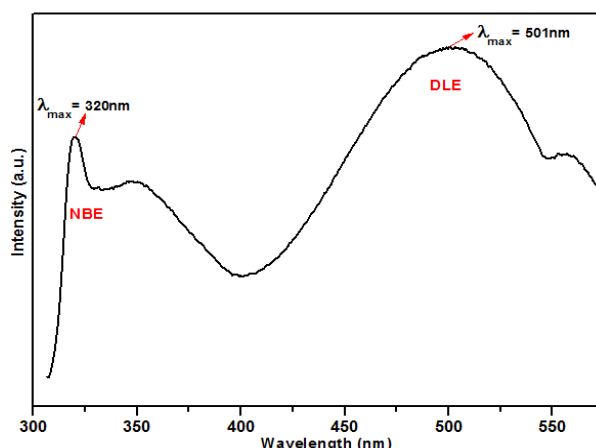


Fig. 5. PL Spectrum of ATO nanoparticles.

The figure 5 shows a strong deep-level emission (DLE) at 501 nm, indicating a high concentration of oxygen vacancies (V_o) in Aluminum-doped Tin Oxide (ATO). This higher concentration of V_o facilitates faster and stronger gas adsorption, improving both the response time and sensitivity of the sensor. Additionally, increased V_o levels lower the activation energy required for gas interactions, allowing the sensor to function efficiently at lower operating temperatures.

4.5. SEM analysis

The irregular shapes of ATO nanoparticles observed in SEM images (Figure 6) suggest a non-uniform growth process or agglomeration, likely due to structural defects or strain introduced during synthesis, potentially influenced by aluminium doping. This doping disrupts the crystal lattice, resulting in irregular particle shapes and a reduction in crystallite size, as confirmed by XRD analysis. From Table 1, the crystallite size varies across different planes, with values ranging from 14.73 nm (for the 110 plane) to 20.19 nm (for the 211 plane) indicate lattice distortions caused by defects such as vacancies, dislocations and grain boundaries [17]. These structural disruptions reduce overall crystallinity and create localized states within the bandgap, modifying the material's electronic and optical properties. The defects act as trap sites for charge carriers, influencing conductivity and charge transport efficiency. The irregular morphology and reduced crystallite size also contribute to an increase in surface area and surface roughness, which enhances the material's reactivity.

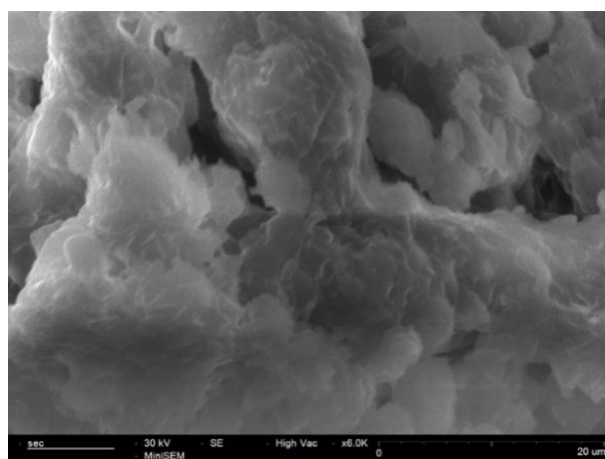


Fig. 6. SEM Image of ATO nanoparticles.

The enhanced surface properties of ATO nanoparticles, including their high surface-to-volume ratio and increased active sites, make them particularly suitable for applications such as gas sensing and photocatalysis. The high surface area improves sensitivity in gas sensing, while the abundant active sites facilitate efficient catalytic processes in photocatalysis.

Fast Fourier Transform (FFT) and Inverse FFT analysis were employed to extract the d-spacing values of ATO nanoparticles. These methods allowed for precise determination of the d-spacing, which was found to be in good agreement with experimental data, validating the structural findings. Structural defects such as stacking faults and dislocations were analyzed by enhancing the FFT derived images with a Sobel filter, accentuating the boundaries of these defects [20]. Further processing of the micrographs generated color images (Figure 7), where clusters of bluish-green lines were identified, corresponding to the positions of stacking faults and dislocations. These defects indicate distortions in the crystal lattice, providing valuable insights into the material's structural integrity and the effects of aluminium doping on the lattice. The detection of these defects helps to understand their role in modifying the material's optical and electronic properties, particularly in relation to photocatalytic and gas sensing applications.

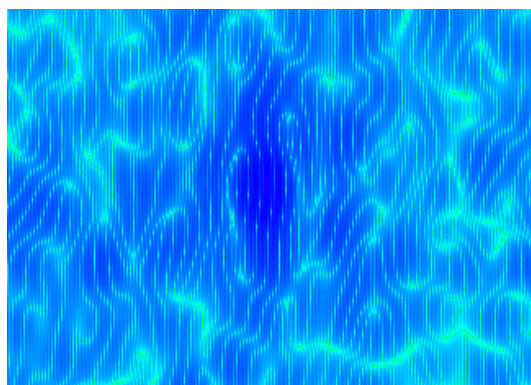


Fig. 7. Defects deduction in ATO nanoparticles.

In parallel, Figure 8 illustrates the 3D surface roughness of ATO nanoparticles, derived from SEM images using image processing tools. The analysis reveals that surface roughness is directly proportional to the material's porosity, suggesting that an increase in surface roughness leads to enhanced porosity [20]. This correlation indicates that surface characteristics, such as roughness and defects, play a critical role in improving the material's reactivity, further enhancing its performance in photocatalysis and gas sensing applications.

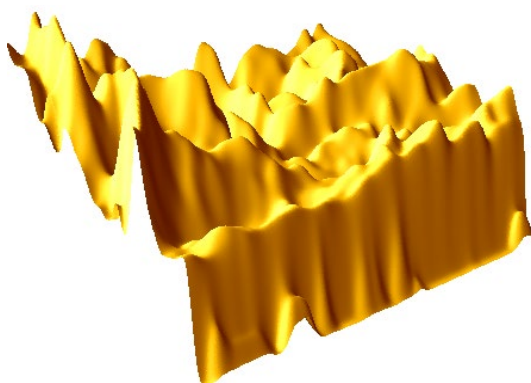


Fig. 8. 3D surface roughness of ATO nanoparticles.

5. Conclusion

In this study, Aluminium doped Tin Oxide (ATO) nanoparticles were successfully synthesized via the sol-gel method and characterized for their structural, morphological and optical properties. XRD analysis confirmed the incorporation of Al³⁺ ions into the SnO₂ lattice, resulting in a lattice contraction, as indicated by the shifts in diffraction peaks to higher 2θ values. SEM revealed a uniform particle distribution with minimal agglomeration, while the optical properties were significantly modified by Al doping, as evidenced by a hypsochromic shift in the absorption edge observed in UV-Visible spectroscopy. FTIR spectroscopy provided insights into the chemical bonding, confirming the successful incorporation of Al without the formation of separate Al₂O₃ phases. PL studies revealed enhanced emission intensities, attributed to defect states arising from oxygen vacancies and the electronic interaction between Al dopants and the SnO₂ lattice. Additionally, image processing techniques were employed to analyze structural defects such as stacking faults and dislocations, which were found to play a role in modifying the material's optical and electronic properties. Surface roughness analysis using image processing tools confirmed that the roughness of ATO nanoparticles is directly proportional to their porosity, suggesting that increased surface roughness enhances porosity, which in turn may improve the material's reactivity and performance in applications such as photocatalysis and gas sensing. The tailored structural and optical properties of ATO nanoparticles, particularly the effects of aluminium doping on lattice strain, defect formation and surface characteristics, position them as promising materials for a wide range of applications, including transparent conductive films, photocatalysis, gas sensors and optoelectronics.

References

- [1] Soussi, A., Haounati, R., Taoufiq, M., Baoubih, S., Jellil, Z., Elfanaoui, A., Markazi, R., Ihlal, A., 2024, *Physica B: Condensed Matter*, 690, p.416242; <https://doi.org/10.1016/j.physb.2024.416242>
- [2] Altaf, U., Ansari, M.Z., Rubab, S., 2024, *Physica B: Condensed Matter*, 676, p.415620; <https://doi.org/10.1016/j.physb.2023.415620>
- [3] Khatun, M.H., Amin, R., Sarker, M.S.I., Shikder, M.R., Islam, S., Shahjahan, M., 2024, *Materials Research Express*, 11(1), p.016102; <https://doi.org/10.1088/2053-1591/ad1d87>
- [4] Teklay, A., 2022. *Optical Properties of undoped and Al, Cu doped Tin oxide (SnO₂) nano Particles (Doctoral dissertation)*.
- [5] Mallick, H.K., Zhang, Y., Pradhan, J., Sahoo, M.P.K., Pattanaik, A.K., 2021, *Journal of Alloys and Compounds*, 854, p.156067; <https://doi.org/10.1016/j.jallcom.2020.156067>
- [6] Butt, M.U., Toheed, M.A., Nasar, R., 2023, *At. Spectrosc*, 45(2), p.2.
- [7] Chakraborty, N., Das, S., Srihari, V., Mondal, D.J., Saha, D., Konar, S., Mishra, A.K., Mondal, S., 2021, *Materials Advances*, 2(11), pp.3760-3769; <https://doi.org/10.1039/D1MA00172H>
- [8] Revathi, V., Rani, S.S., Balamurugan, M., Manikumar, T., Sivakumar, S., Sangeetha, B., 2024, *Digest Journal of Nanomaterials & Biostructures (DJNB)*, 19(3); <https://doi.org/10.15251/DJNB.2024.193.1265>
- [9] Sridevi, K.P., Revathi, V., Sangeetha, P., Manjunatha, B., Sivakumar, S., 2024, *Digest Journal of Nanomaterials & Biostructures (DJNB)*, 19(1); <https://doi.org/10.15251/DJNB.2024.191.263>
- [10] Sridevi, K.P., Prasad, L.G., Sangeetha, B., Sivakumar, S., 2022, *Journal of Ovonic Research*, 18(3), pp.453-464; <https://doi.org/10.15251/JOR.2022.183.453>
- [11] Vetrivel, M., Jagadeeshwaran, A., Sangeetha, B., 2024, *Journal of Ovonic Research*, 20(6), pp. 841 - 849. <https://doi.org/10.15251/JOR.2024.206.841>
- [12] Kannan, K., Manjunatha, B., Marimuthu, T., Sangeetha, P., 2025, *Chalcogenide Letters*, 22(2), pp. 167 – 175. <https://doi.org/10.15251/CL.2025.222.167>

- [13] Purushotham, S., Ramkumar, G., Kannan, V., Kumar, A., 2023, *Physica Scripta*, 98(12), p.125951. DOI .10.1088/1402-4896/ad0aea
- [14] Saravanan, S.P., Meeran, M.N., Sankar, A., Thillaikkarasi, D., 2025, *Journal of Inorganic and Organometallic Polymers and Materials.*, pp.1-11; DOI: 10.1007/s10904-025-03786-5
- [15] Kaarthik, K., Vivek, C., Balraj, B., 2024, *Optical Materials*, p.116090; DOI: 10.1016/j.optmat.2024.116090
- [16] Altaf, U., Ansari, M.Z., Rubab, S., 2023, *Materials Chemistry and Physics*, 297, p.127304; <https://doi.org/10.1016/j.matchemphys.2023.127304>
- [17] Suvarna, T., Reddy, K.G., Mohan, V.M., Lavanya, G., Reddy, M.R., Vardhani, C.P., 2024, *Inorganic Chemistry Communications*, p.112748; <https://doi.org/10.1016/j.inoche.2024.112748>
- [18] Sharma, V., 2020, *Tin Oxide Materials* (pp. 61-99). Elsevier; <https://doi.org/10.1016/B978-0-12-815924-8.00004-9>
- [19] Aguir, K., Bernardini, S., Lawson, B., Fiorido, T., 2020, *Tin oxide materials* (pp. 219-246). Elsevier; <https://doi.org/10.1016/B978-0-12-815924-8.00008-6>
- [20] Stiefel, M., Müller, M., Bachmann, B.I., Guitar, M.A., Nayak, U.P., Mücklich, F., 2024, *MRS Communications*, pp.1-9; <https://doi.org/10.1557/s43579-024-00549-0>